Sustainable Energy & Fuels

ROYAL SOCIETY OF CHEMISTRY

PAPER

View Article Online
View Journal | View Issue

Cite this: *Sustainable Energy Fuels*, 2020, **4**, 3604

Reasonable construction of Fe_3O_4/Ni@N-RGO nanoflowers as highly efficient counter electrodes for dye-sensitized solar cells

Haifeng Xu *[a] and Zhong Jin *[b]

Received 26th March 2020
Accepted 22nd April 2020

DOI: 10.1039/d0se00494d

rsc.li/sustainable-energy

The rational design of high-performance yet low-cost counter electrodes (CEs) with exceptional catalytic activity for the I^-/I_3^- redox couple and excellent corrosion resistance is of great importance for dye-sensitized solar cells (DSSCs). Metal nickel-based CEs have super electrical conductivity for the oxidation of I^-, but they lack the ability to restore I_3^-, leading to relatively poor photoelectric conversion efficiency (PCE). Herein, we propose the design and development of a novel nanostructured CE material composed of hierarchical porous Fe_3O_4 nanoflowers decorated with Ni nanoparticles and wrapped by N-doped reduced graphene oxide nanosheets (Fe_3O_4/Ni@N-RGO). The as-prepared multi-component electrode material was applied as a CE for DSSCs, attaining high efficiency and excellent stability. The PCE of Fe_3O_4/Ni@N-RGO based DSSCs reaches 8.96%, which is superior to those based on Fe_3O_4 (7.92%) or Pt (7.87%). Moreover, the Fe_3O_4/Ni@N-RGO electrode also displays ultrahigh corrosion resistance under complicated working conditions. The advantages of the Fe_3O_4/Ni@N-RGO electrode material indicate its good potential for application in DSSCs as a high-performance and inexpensive CE material.

1. Introduction

Dye-sensitized solar cells (DSSCs) are promising candidates in the field of photovoltaic devices, owing to their low-cost production, simple fabrication, and relatively high stability.[1–4] In general, a DSSC is made of three key components: a dye-sensitized TiO_2 photoanode, a counter electrode (CE) and a redox-reversible electrolyte.[5–12] The main function of the CE is to stimulate the reduction of I_3^- to I^- ions and achieve electric conductance in the whole system.[13,14] In the whole photoelectric conversion process, the CE plays an important role in improving the catalytic activity of the I^-/I_3^- redox couple and expediting the electron transfer from the external circuit to the DSSC system.[15–18] A suitable CE should have some fundamental properties, such as high electrical conductivity, good electrocatalytic activity for the regeneration of redox couples and long-term stability in the electrolyte system.[19] The conventional CE material in DSSCs is Pt, which has good characteristics for electrocatalysis.[20–24] However, the application of Pt-based CEs is limited by their high cost and low abundance. Beside, Pt may react with I^- ions to produce PtI_4 in iodine electrolyte according to Hauch's theoretical calculation, leading to reduced service life.[25,26] These reasons extremely hamper the commercial application of DSSCs. Therefore, searching for earth-abundant and inexpensive CE materials is of great importance for alternative Pt. Among numerous prospective candidates, transition metal oxides are extremely abundant in nature and have reasonable catalytic activity, but their applications are seriously limited by their low conductivity and poor stability, which may lead to severe decay of capacity over long-term cycling when fully exposed to electrolytes. These shortcomings severely hamper the application of transition metal oxides as CE materials in the field of DSSCs. To solve these problems, great efforts have been devoted to improving the electrochemical performance of oxide-based CEs by constructing nanostructured heterojunctions and decorating with co-catalysts.

Herein, we report a two-step strategy to prepare a novel composite CE material consisting of hierarchical porous Fe_3O_4 nanoflowers decorated with Ni nanoparticles and wrapped by N-doped reduced graphene oxide nanosheets (Fe_3O_4/Ni@N-RGO) for DSSCs (Scheme 1). The mesoporous Fe_3O_4 nanoflowers were firstly synthesized by a facile solvothermal process. The flower-like nanostructure can offer a 3D porous scaffold with a large specific surface area for loading Ni nanoparticles and N-doped graphene nanosheets. The as-obtained Fe_3O_4/Ni@N-RGO composite can afford high catalytic activity, excellent electrical conductivity and abundant nanopores to interact with I_3^- ions. Benefiting from these favorable effects, DSSCs

[a]*Key Laboratory of Spin Electron and Nanomaterials of Anhui Higher Education Institutes, School of Mechanical and Electronic Engineering, Suzhou University, Suzhou 234000, China. E-mail: xuhaifeng@ahsztc.edu.cn*

[b]*Key Laboratory of Mesoscopic Chemistry of MOE, Jiangsu Key Laboratory of Advanced Organic Materials, School of Chemistry and Chemical Engineering, Nanjing University, Nanjing 210023, China. E-mail: zhongjin@nju.edu.cn*

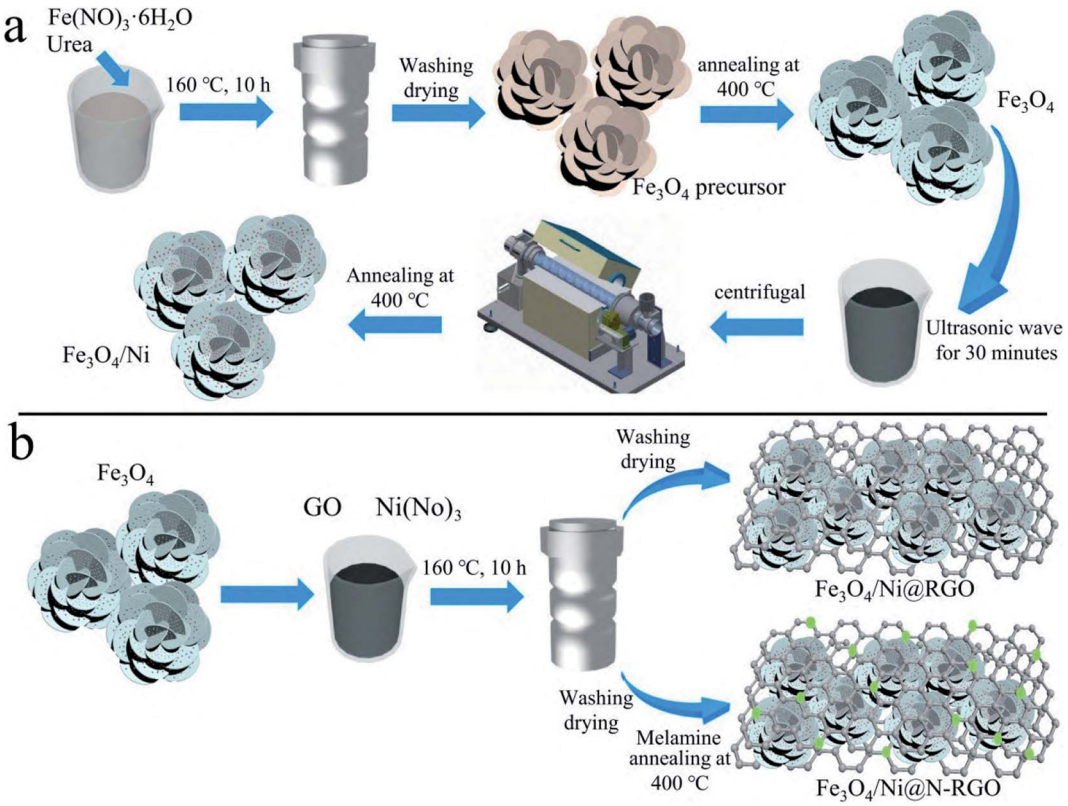

Scheme 1 (a) Schematic reaction route for the preparation of the Fe_3O_4/Ni composite. (b) Schematic reaction routes for the preparation of Fe_3O_4/Ni@RGO and Fe_3O_4/Ni@N-RGO composites.

assembled with Fe_3O_4/Ni@N-RGO CEs exhibit a high photoelectric conversion efficiency (PCE) of 8.96%, which is superior to that of Pt CEs. Furthermore, the electrocatalytic stability of the Fe_3O_4/Ni@N-RGO CE is better than that of Pt, thus being beneficial to serve as a promising CE material for low-cost and Pt-free DSSCs.

2. Experimental section

2.1 Synthesis of Fe_3O_4 nanoflowers

The Fe_3O_4 nanoflower precursor was prepared *via* a one step hydrothermal method. In a word, (0.95 g) $FeCl_3 \cdot 6H_2O$ and (0.4 g) CH_3COONa were added to pure $C_2H_6O_2$ (40 mL) and kept under vigorous stirring. Another 40 mL $C_2H_6O_2$ solution containing (0.4 g) $C_6H_5Na_3O_7 \cdot 2H_2O$ and (0.2 g) COH_4N_2 was prepared and continuously stirred for 30 min. The two solutions were uniformly mixed and then transferred into Teflon-lined stainless-steel autoclaves, which were heated at 180 °C for 12 h to form nanoflowers. Finally, pure Fe_3O_4 nanoflowers were obtained by annealing the precursor.

2.2 Synthesis of Fe_3O_4/Ni and Fe_3O_4/Ni@RGO and Fe_3O_4/Ni@N-RGO

For Fe_3O_4/Ni nanocomposites, (0.2 g) Fe_3O_4 nanoflowers were poured into nickel nitrate solution and kept under mechanical stirring for 24 hours. Subsequently, the samples were collected by centrifugation and then dried at 50 °C for 12 h. These samples were calcined at 700 °C for 2 h to form Fe_3O_4/Ni nanocomposites. For Fe_3O_4/Ni@N-RGO nanocomposites, (0.2 g) Fe_3O_4 nanoflowers and 0.06 g GO were added into nickel nitrate solution and ultrasonicated to form a homogeneous solution. Then the samples were obtained by centrifugation and dried at 50 °C for 12 h. These samples were calcined at 700 °C for 2 h. Fe_3O_4/Ni@RGO nanocomposites were obtained. Moreover, these samples and tripolycyanamide were mixed and calcined at 700 °C for 2 h to form Fe_3O_4/Ni@N-RGO nanocomposites.

2.3 Characterization and measurements

Photocurrent density–voltage (*J*–*V*) curves showing the photovoltaic effect were obtained using a solar light simulator under an illumination of 100 mW cm^{-2}, AM 1.5 and using a digital source meter (Keithley 2410). Cyclic voltammetry (CV) curves were recorded in the range from −0.4 to 1.1 V at a scan rate of 25 mV s^{-1} in a supporting electrolyte consisting of 10 mM LiI, 1 mM I_2, and 100 mM $LiClO_4$ in acetonitrile and the measurements were carried out in a three-electrode system. A Pt thin film was used as the CE and Ag/AgCl with saturated KCl solution was used as the reference electrode. In DSSCs, a symmetrical cell is widely used in EIS and Tafel polarization measurements. Electrochemical impedance spectroscopy (EIS) of symmetrical cells was performed in a frequency range of 0.1–10^6 Hz and at an alternating current voltage amplitude of 10 mV. Tafel polarization measurements were also performed in a symmetrical cell

under quasi stationary conditions within the voltage range of −1 to 1 V at a scan rate of 50 mV s^{-1}. EIS and Tafel measurements were carried out in a dark environment.

The surface morphologies of the CEs were observed *via* a field-emission scanning electron microscope (JSM-6701F, JEOL accelerating voltage of 5 kV), transmission electron microscope (TEM, JEOL-2010, operating voltage of 200 kV), and high-resolution TEM (HRTEM, JEOL-2010). All samples were prepared by depositing a drop of diluted suspensions in ethanol on a carbon-film-coated copper grid. The crystalline structures of N-CHS/Ni_3B/NiO and N-CHS/Ni_3B/NiO/RGO powders were recorded *via* a Raman spectrometer and a Rigaku/Max-3A X-ray diffractometer with Cu Kα radiation (λ = 1.54178 Å). X-ray photoelectron spectroscopy was conducted using a Smart Lab 9 KW to study the chemical states.

3. Results and discussion

The crystal structures of Fe_3O_4 nanoflowers, Fe_3O_4@Ni, Fe_3O_4/Ni@RGO and Fe_3O_4/Ni@N-RGO composites were observed by powder X-ray diffraction (XRD), as displayed in Fig. 1a. The typical diffraction peaks of these samples located at 18.4°, 30.2°, 35.5°, 37.1°, 43.2°, 53.1°, 57.1°, 62.8° and 87.1° can be well indexed to the (111), (220), (311), (222), (400), (422), (511), (440) and (642) crystal planes of Fe_3O_4 (JCPDS no. 75-0033), corresponding well to the standard crystallographic spectra of Fe_3O_4. Meanwhile, the characteristic peaks of Ni species located at 44.5°, 51.8° and 76.4° can be well indexed to the (111), (200) and (220) planes of metal Ni (JCPDS no. 40-0850). The XRD pattern of the Fe_3O_4/Ni@RGO composite demonstrates the characteristic peaks of Fe_3O_4 (311) and Ni (111) planes, confirming the co-presence of Fe_3O_4 nanoflowers and Ni nanoparticles. A broad peak at 24° can be assigned to the (002) planes of RGO in the Fe_3O_4/Ni@RGO composite. The presence of Fe_3O_4, Ni and RGO in Fe_3O_4/Ni@RGO and Fe_3O_4/Ni@N-RGO composites can be further established by Raman spectroscopy, as shown in Fig. 1b. It can be clearly found that the characteristic peaks of Fe_3O_4 are located at 214.8, 278.4 and 386.5 cm^{-1}. The feature peaks of Ni are located at 469.9, 548.2 and 575.8 cm^{-1}. The two characteristic D and G bands at 1357.8 and 1598.4 cm^{-1} in the Raman

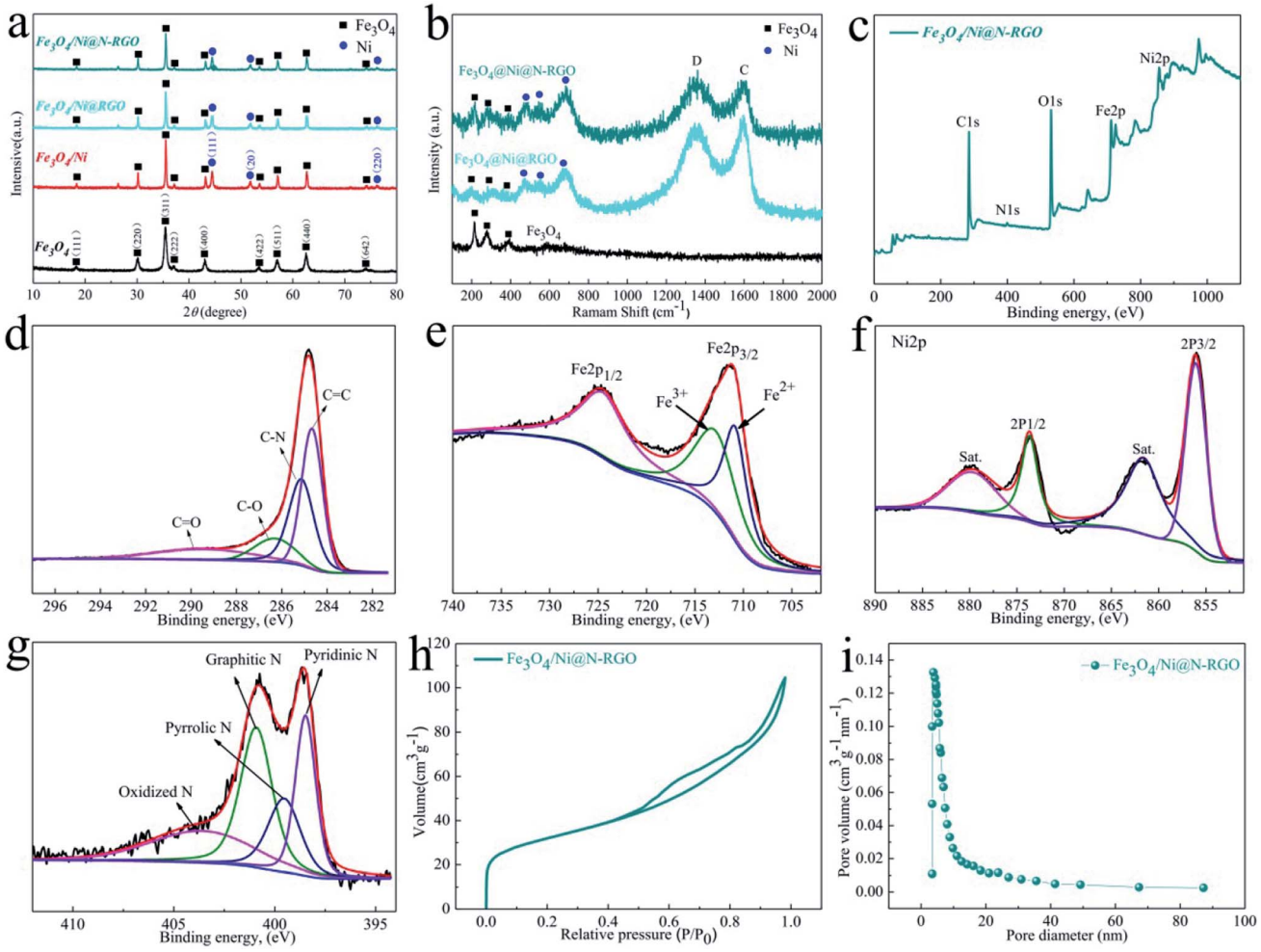

Fig. 1 (a) XRD patterns and (b) Raman spectra of Fe_3O_4 nanoflowers, Fe_3O_4/Ni, Fe_3O_4/Ni@RGO and Fe_3O_4/Ni@N-RGO composites. (c) Survey XPS spectra of Fe_3O_4/Ni@N-RGO. (d) C 1s, (e) Fe 2p, (f) Ni 2p and (g) N 1s spectra of Fe_3O_4/Ni@N-RGO. (h) N_2 adsorption–desorption isotherms and (i) corresponding pore size distribution of Fe_3O_4/Ni@N-RGO.

spectra of Fe_3O_4/Ni@RGO and Fe_3O_4/Ni@N-RGO composites are assigned to the vibration of sp^2-bonded (graphitic) and sp^3-bonded (defective/amorphous) carbon atoms in RGO.[27–29] The I_D/I_G of the Fe_3O_4/Ni@N-RGO composite is measured to be 1.12, which is higher than that of Fe_3O_4/Ni@RGO (0.96), signifying the existence of more defects in RGO owing to the introduction of nitrogen heteroatoms.[30]

X-ray photoelectron spectroscopy (XPS) was carried out to assess the typical signals of C, N, O, Fe and Ni elements in the Fe_3O_4/Ni@N-RGO composite, as shown in Fig. 1c. The corresponding C 1s spectrum of Fe_3O_4/Ni@N-RGO is presented in Fig. 1d. The peaks located at 284.6, 285.2, 286.3 and 289.8 eV are assigned to the C=C, C–N, C–O and C=O bonds. In Fig. 1e, the peaks at around 711.4 and 724.8 eV can be indexed to Fe $2p^{3/2}$ and Fe $2p^{1/2}$ energy bands. The two major peaks at 713.3 eV and 710.9 eV are derived from the Fe^{3+} and Fe^{2+} species in Fe_3O_4, respectively. The characteristic peak of Ni(0) can be detected in the Ni 2p spectrum (Fig. 1f), indicating that metallic Ni nanoparticles were successfully loaded on Fe_3O_4 nanoflowers.[31] In the N 1s spectrum displayed in Fig. 1g, the peaks located at 398.5 eV, 399.5 eV, 400.9 eV and 403.8 eV indicate the presence of four types of N species (pyridinic N, pyrrolic N, graphitic N, and oxidized N, respectively), verifying the introduction of N atoms into the carbon matrix.[32] The N heteroatoms can effectively modify the electronic structure of RGO, so that the electric conductivity could be further enhanced. Therefore, the reduction of I_3^- can be further promoted, which can be confirmed by the subsequent electrochemical studies.[33,34]

The Brunauer–Emmett–Teller (BET) method was employed to assess the porosity of the Fe_3O_4/Ni@N-RGO composite, as displayed in Fig. 1h. The specific surface area of the Fe_3O_4/Ni@N-RGO composite is measured to be 87 $m^2\ g^{-1}$, and the average pore size distribution is about 8.2 nm (Fig. 1i). The existence of N-RGO can increase the number of active sites for electrocatalysis and shorten the electronic transmission path, thus being conducive to the device performances of DSSCs.[35,36]

The morphology and microstructure of the samples were identified by scanning electron microscopy (SEM) and transmission electron microscopy (TEM). The SEM images of Fe_3O_4 nanoflowers display a uniform flower-like structure with an average size of ~2 μm, as shown in Fig. 2a and b. At high magnification, it can be clearly found that there are many nanoholes on the surface of Fe_3O_4 nanoflowers (Fig. 2b), which is helpful for the loading of Ni particles and also conducive to the ion/electron transport at the electrode/electrolyte interface. The Fe_3O_4 nanoflowers exhibit a hollow spherical structure decorated with numerous porous thin nanoflakes, as shown in the TEM images (Fig. 2c and d), which is conducive to offering a large electrochemical surface area and facilitating the adsorption of electrolyte. The microstructures of Fe_3O_4/Ni and Fe_3O_4/Ni@N-RGO were observed by SEM and TEM. As shown in Fig. 3a, the Fe_3O_4/Ni composite shows many particles loaded on Fe_3O_4 nanoflowers, indicating the successful introduction of Ni particles to form the Fe_3O_4/Ni composite. N-RGO was further utilized to wrap up Fe_3O_4/Ni and form the Fe_3O_4/Ni@N-RGO composite, as shown in Fig. 3b. The internal structure of the Fe_3O_4/Ni@N-RGO composite is presented by TEM at different magnifications. As shown in Fig. 3c, N-RGO can also be clearly identified, as indicated by the red arrow. The Fe_3O_4/Ni@N-RGO composite shows a hierarchical hollow structure, similar to the precursor Fe_3O_4 nanoflowers. The Ni nanoparticles are uniformly distributed on the surface of Fe_3O_4 nanoflowers, as shown in the high-

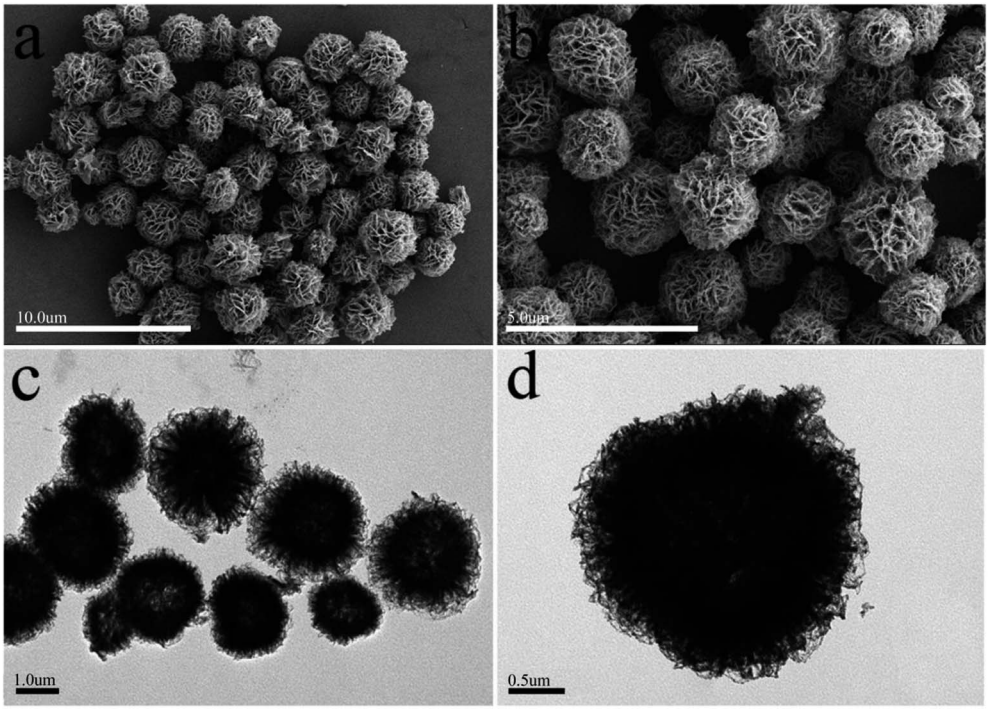

Fig. 2 (a and b) SEM and (c and d) TEM images of Fe_3O_4 nanoflowers.

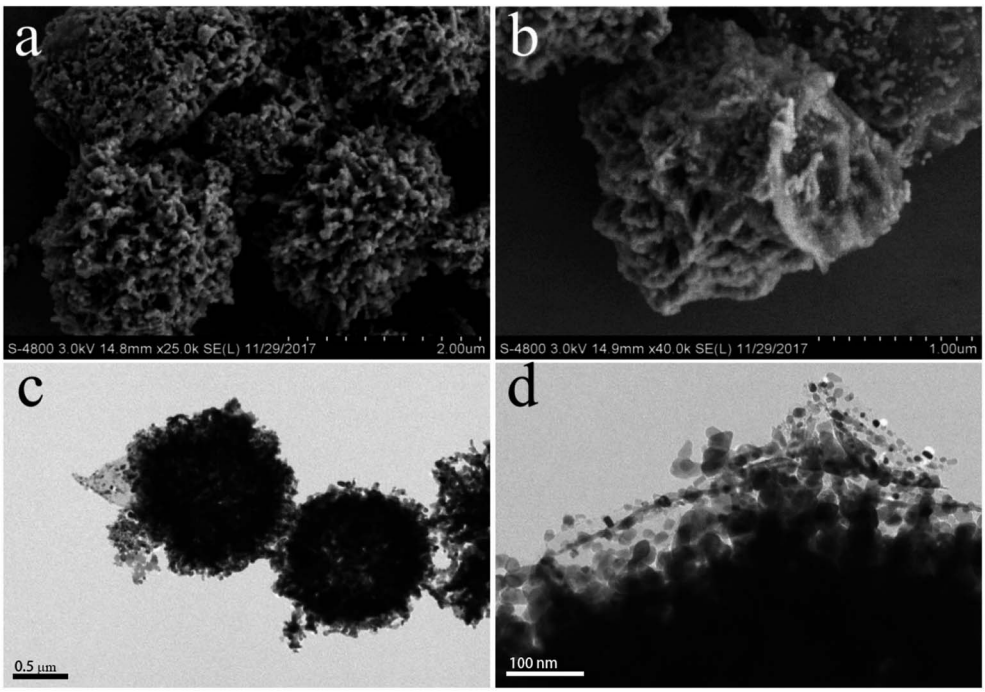

Fig. 3 (a and b) SEM and (c and d) TEM images of Fe_3O_4/Ni@N-RGO composite.

magnification TEM image (Fig. 3d). Meanwhile, the coating of N-RGO nanosheets is helpful to stabilize the nickel nanoparticles during the electrocatalytic processes. The combined and synergistic effect of these ternary substances (Fe_3O_4, Ni and N-RGO) is beneficial to provide more active sites and facilitate interactions at electrode/electrolyte interfaces, thus efficiently enhancing the electrochemical performances.[37–40]

The electrochemical properties of the as-prepared samples were further assessed by electrochemical measurements. The catalytic activities of the above samples and Pt electrode for I_3^-/I^- conversion were assessed by cyclic voltammogram (CV) measurements carried out in a standard three-electrode system with an identical scan rate (25 mV s^{-1}), as displayed in Fig. 4a. It can be clearly found that each CV curve shows two pairs of redox peaks ranging from −0.4 to −1.0 V, indicating that each material exhibits certain catalytic properties.[41,42] The redox peak pair on the left is denoted as Ox1/Red1, and the peak pair on the right is denoted as Ox2 and Red2. The values of oxidation and reduction peaks are shown in Fig. 4a and b. The major function of the CE is to collect electrons and catalyze the following reaction: $I_3^- + 2e^- \rightarrow 3I^-$, and therefore the reaction kinetics relies on the electronic structure of the CE material.[43] The higher current densities of the redox peaks in the CV curve of the Fe_3O_4/Ni@N-RGO composite indicate its better catalytic performance. The peak-to-peak separation (E_{pp}) between Ox1 and Red1 peaks can be used to evaluate the catalytic performance for I_3^-/I^- conversion, as summarized in Fig. 4d. The Fe_3O_4/Ni@N-RGO composite shows the lowest value of E_{pp} among all the samples, presenting its best reaction kinetics and catalytic performance.

Electrochemical impedance spectra (EIS) and Tafel polarization plots were obtained to further evaluate the catalytic performance for I^-/I_3^- conversion on the electrode surface. The EIS analysis was performed in symmetric cells assembled by two identical electrodes made of the samples.[44–46] The corresponding equivalent circuits of the Nyquist diagrams are shown in the inset of Fig. 5a. The test results of EIS can mirror the electronic conductivity and interfacial charge transfer properties of the cell. It can be found that all the EIS curves in Fig. 5a exhibit two semicircles. The Nernst diffusion impedance in the electrolyte (Z_N) is revealed by the right semicircle.[47] The intersection of the x-axis and the left semicircle represents the series resistance (R_s).[48] The resistance of the FTO substrate and the contact resistance between the interface of the FTO substrate and electrode material have little effect on R_s. Hence, the value of R_s mainly depends on the intrinsic resistance of the electrode material. The size of the left semicircle discloses the value of charge transfer resistance (R_{ct}) at the electrode/electrolyte interface.[49] The R_{ct} has important influence on the electrocatalytic performance of the electrode material for the reduction of I_3^-. The values of R_s and R_{ct} of all the samples are summarized in Table 1. The R_{ct} values of the samples can be sorted in the following order: Pt (0.51 Ω) > Fe_3O_4 (0.49 Ω) > Fe_3O_4/Ni (0.21 Ω) > Fe_3O_4/Ni@RGO (0.17 Ω) > Fe_3O_4/Ni@N-RGO (0.16 Ω), as displayed in Fig. 5b. Among them, it is clear that the Fe_3O_4/Ni@N-RGO composite exhibits the minimum value of R_{ct}, verifying its outstanding catalytic performance.

The Tafel plots at the cathodic branch can be used to further evaluate the catalytic performance of electrode materials and are presented in Fig. 5c, which presents two vital parameters: the exchange current density (J_0) and the limiting diffusion current density (J_{lim}).[50] The J_0 and J_{lim} values can be calculated according to the following equations:

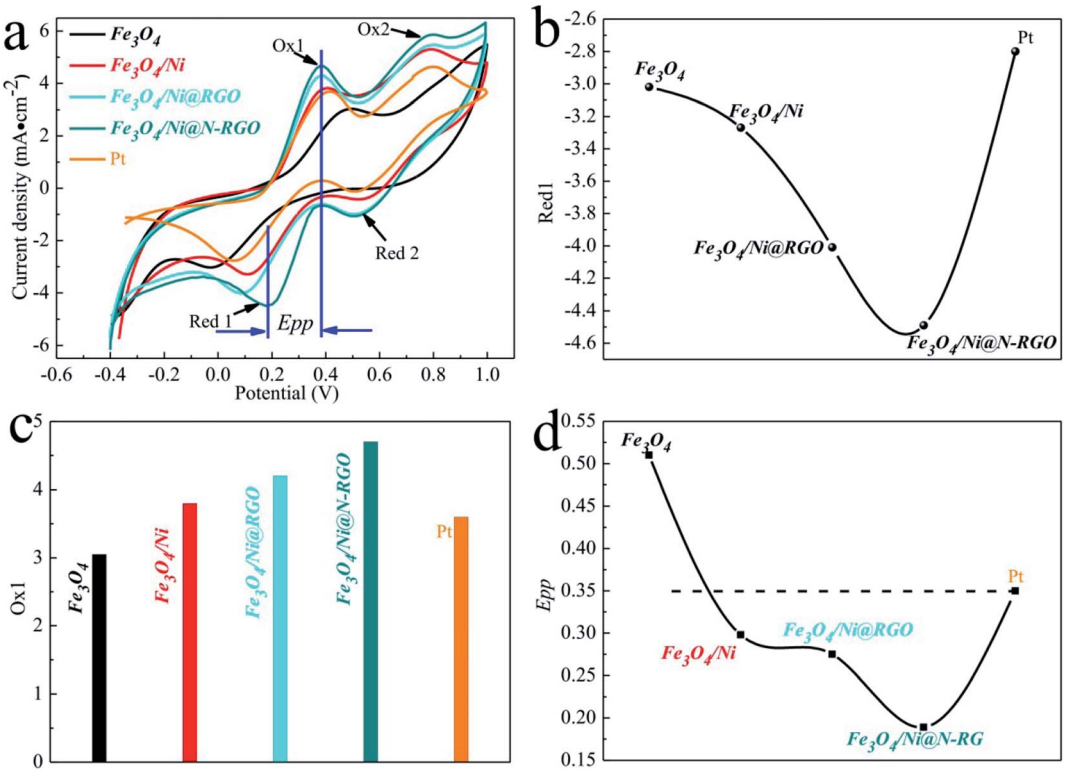

Fig. 4 (a) CV curves of Fe_3O_4 nanoflowers, Fe_3O_4/Ni, Fe_3O_4/Ni@RGO, Fe_3O_4/Ni@N-RGO and Pt electrodes in the I^-/I_3^--containing electrolyte. (b) Current densities of (b) Red1 and (c) Ox1 peaks of all the samples measured in (a). (d) The E_{pp} values of all the samples.

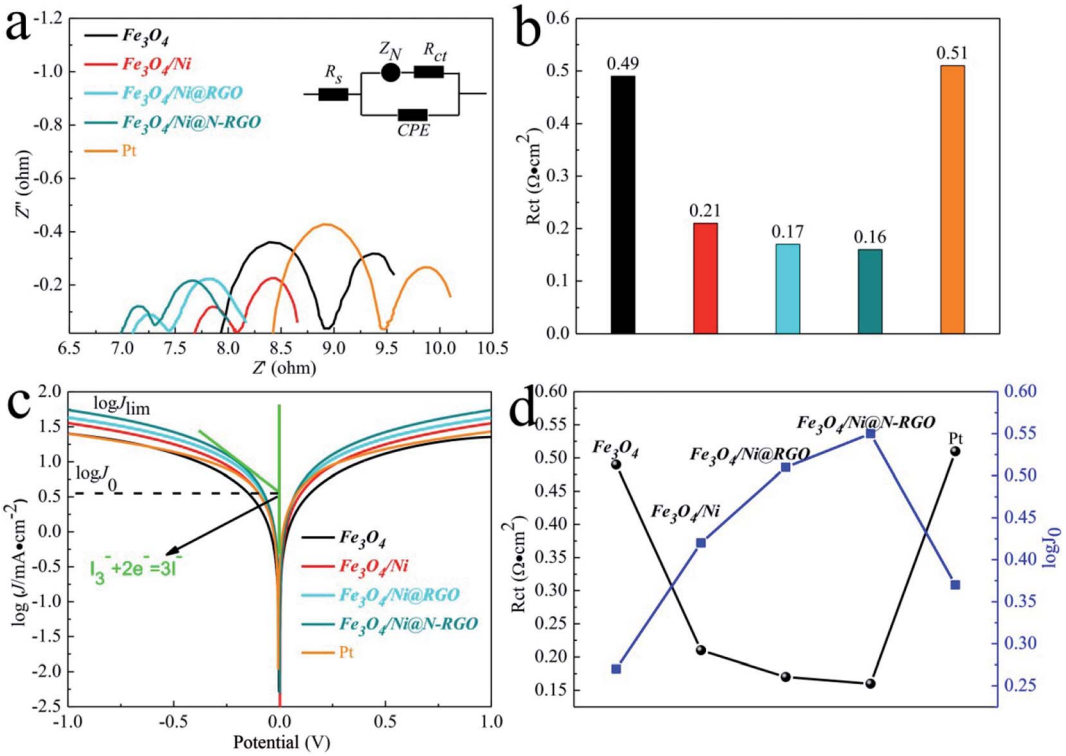

Fig. 5 (a) Nyquist plots and (b) R_{ct} values of the DSSCs using Fe_3O_4 nanoflowers, Fe_3O_4/Ni, Fe_3O_4/Ni@RGO, Fe_3O_4UFM@N-RGO and Pt as the CEs. (c) Tafel polarization curves. (d) The association diagram of R_{ct} and log(J_0).

Table 1 Electrochemical parameters derived from the EIS and Tafel curves of the DSSCs based on different CEs recorded under the same conditions

CEs	R_s (Ω cm^2)	R_{ct} (Ω cm^2)	J_0 (mA cm^{-2})	J_{lim} (mA cm^{-2})	E_{pp} (V)
Fe_3O_4	7.9	0.49	0.27	1.40	0.51 ± 0.01
Fe_3O_4/Ni	7.7	0.21	0.42	1.52	0.30 ± 0.01
Fe_3O_4/Ni@RGO	7.1	0.17	0.51	1.62	0.28 ± 0.01
Fe_3O_4/Ni@N-RGO	6.9	0.16	0.55	1.72	0.19 ± 0.01
Pt	8.4	0.51	0.37	1.40	0.35 ± 0.01

$$J_0 = \frac{RT}{nFR_{ct}} \quad (1)$$

$$J_{lim} = \frac{2neDCN_A}{l} \quad (2)$$

In eqn (1), R represents the gas constant, T represents the temperature, F represents the Faraday constant, and n represents the number of electrons exchanged in the reaction at the CE interface and the electrolyte. In eqn (2), e is the elementary charge, C is the concentration of the I_3^- ions, D is the diffusion coefficient of I_3^-, N_A is the Avogadro constant, and l is the electrode spacing. The corresponding J_0 and J_{lim} values of the samples are listed in Table 1. In general, the higher J_0 and J_{lim} values suggest better catalytic performance.[51,52] Moreover, through the measurements of EIS and Tafel plots, it is revealed that the value of J_0 is inversely proportional to the R_{ct}, as presented in Fig. 5d. It is noteworthy that the Fe_3O_4/Ni@N-RGO composite possesses the highest J_0 (0.55 mA cm^{-2}) and J_{lim} (1.74 mA cm^{-2}) values among the samples, indicating its superior catalytic ability for the reduction of I_3^-. In brief, the results of CV, EIS and Tafel measurements consistently show that the Fe_3O_4/Ni@N-RGO composite possesses high performance for electrocatalytic I^-/I_3^- conversion.[53]

The photovoltaic parameters of DSSCs based on different CE materials were measured and are summarized in Fig. 6a. The density–voltage (J–V) curves were recorded to access the overall performance of DSSCs. The PCE values of these DSSCs are

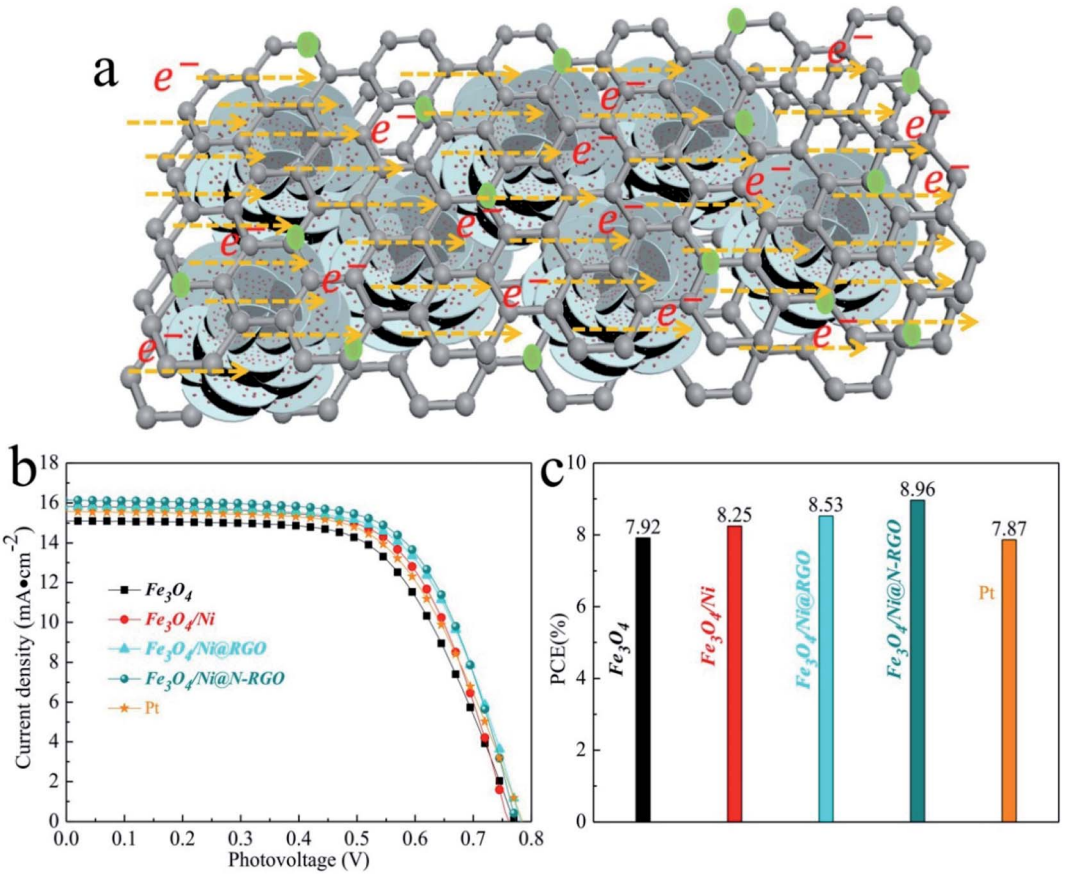

Fig. 6 Schematic diagram of the electron transport and I_3^-/I^- conversion on the Fe_3O_4/Ni@N-RGO electrode. (b) J–V curves and (c) PCEs of the DSSCs with different CEs.

Table 2 Photovoltaic parameters of the DSSCs based on different CEs recorded under the same conditions

CEs	J_{sc} (mA cm^{-2})	V_{oc} (V)	FF (%)	PEC (%)
Fe_3O_4	15.1	0.770	68.11	7.92
Fe_3O_4/Ni	15.7	0.760	69.14	8.25
Fe_3O_4/Ni@RGO	15.8	0.775	69.66	8.53
Fe_3O_4/Ni@N-RGO	16.5	0.778	69.79	8.96
Pt	15.6	0.780	64.66	7.87

calculated with the corresponding short-circuit (J_{sc}), open-circuit voltage (V_{oc}), and fill factor (FF), as listed in Table 2. The DSSC based on the Fe_3O_4/Ni@N-RGO composite CE exhibits a high short-circuit (J_{sc}) of 16.5 mA cm^{-2}, open-circuit voltage (V_{oc}) of 0.778 V and FF of 69.75%, which are remarkable among all the samples. As a result, the PCE of the DSSC based on Fe_3O_4/Ni@N-RGO reached 8.96%, which is higher than that of Fe_3O_4 (7.92%), Fe_3O_4/Ni (8.25%), Fe_3O_4/Ni@RGO (8.53%) and metal Pt (7.87%). The high PCE can be ascribed to the hollow and nanoporous structure of Fe_3O_4/Ni@N-RGO, which can facilitate the filtration of electrolyte and shorten the ion transfer pathway.[54,55] The introduction of N-RGO can reduce the charge transfer resistance. Furthermore, the synergistic effect of these components is conducive to improving the catalytic activity of Fe_3O_4/Ni@N-RGO.

4. Conclusions

In summary, the Fe_3O_4/Ni@N-RGO composite with hierarchical and flower-like nanoarchitecture was used as a novel CE material to enhance the device performances of DSSCs. The hollow and porous structure of Fe_3O_4 nanoflowers was exploited strategically for the loading of highly active Ni nanoparticles and conductive N-RGO nanosheets, favorable for the electrocatalytic properties and ion transport at the electrode/electrolyte interface. The rational combination of these complementary compositions can effectively improve the photovoltaic parameters of DSSCs. The PCE of the DSSC based on the Fe_3O_4/Ni@N-RGO composite achieves a high PCE of 8.96%, which is higher than those based on the control samples and Pt electrode. This study highlights the importance of the synergetic catalytic properties of transition metal oxides, transition metal nanoparticles and N-RGO nanosheets. We expect that this work can display a hopeful strategy to reasonably design high-performance electrode materials for DSSCs and other electrocatalytic devices.

Conflicts of interest

The authors declare no competing financial interest.

Acknowledgements

This work is supported financially by the Outstanding Youth Talents in Anhui Provincial Education Department (2019gxbjZD43), the College Natural Science Key Foundation of Anhui Province (No. KJ2018A0453), the Academic Technical Leader of Suzhou University (No. 2018xjxs03, 2016XJXS03), the Innovative Research Team of Anhui Provincial Education Department (No. 2016SCXPTTD), and the Key Discipline of Material Science and Engineering of Suzhou University (No. 2017XJZDXK3). This work is also supported by the National Key R&D Program of China (2017YFA0208200), the Projects of NSFC (21872069, 51761135104), the Natural Science Foundation of Jiangsu Province (BK20180008), and the Fundamental Research Funds for the Central Universities of China (0205-14380188).

References

1 Q. Tang, W. Zhu, B. He and P. Yang, *ACS Nano*, 2017, **11**, 1540–1547.
2 Y. Kim, K. Bicanic, H. Tan, O. Ouellette, B. R. Sutherland, F. P. Garcia de Arquer, J. W. Jo, M. Liu, B. Sun, M. Liu, S. Hoogland and E. H. Sargent, *Nano Lett.*, 2017, **17**, 2349–2353.
3 M. Ye, X. Wen, M. Wang, J. Iocozzia, N. Zhang, C. Lin and Z. Lin, *Mater. Today*, 2015, **18**, 155–162.
4 R. Li, X. Zhu, Q. Fu, G. Liang, Y. Chen, L. Luo, M. Dong, Q. Shao, C. Lin, R. Wei and Z. Guo, *Chem. Commun.*, 2019, **55**, 2493–2496.
5 B. Kirubasankar, V. Murugadoss, J. Lin, T. Ding, M. Dong, H. Liu, J. Zhang, T. Li, N. Wang, Z. Guo and S. Angaiah, *Nanoscale*, 2018, **10**, 20414–20425.
6 M. Liu, Z. Yang, H. Sun, C. Lai, X. Zhao, H. Peng and T. Liu, *Nano Res.*, 2016, **9**, 3735–3746.
7 H. J. Zhang, X. T. Li, X. F. Meng, S. T. Zhou, G. Yang and X. M. Zhou, *J. Phys.: Condens. Matter*, 2019, **31**, 125301.
8 A. Bansal, H. Liu, M. K. Jayakumar, S. Andersson-Engels and Y. Zhang, *Small*, 2016, **12**, 1732–1743.
9 J. Yao, K. Zhang, W. Wang, X. Zuo, Q. Yang, H. Tang, M. Wu and G. Li, *Nanoscale*, 2018, **10**, 7946–7956.
10 C. Hou, Z. Tai, L. Zhao, Y. Zhai, Y. Hou, Y. Fan, F. Dang, J. Wang and H. Liu, *J. Mater. Chem. A*, 2018, **6**, 9723–9736.
11 H. Huang, R. Cao, S. Yu, K. Xu, W. Hao, Y. Wang, F. Dong, T. Zhang and Y. Zhang, *Appl. Catal., B*, 2017, **219**, 526–537.
12 F. Du, X. Zuo, Q. Yang, G. Li, Z. Ding, M. Wu, Y. Ma and K. Zhu, *J. Mater. Chem. C*, 2016, **4**, 10323–10328.
13 I. P. Liu, W. H. Lin, C. M. Tseng-Shan and Y. L. Lee, *ACS Appl. Mater. Interfaces*, 2018, **10**, 38900–38905.
14 P.-J. Chang, K.-Y. Cheng, S.-W. Chou, J.-J. Shyue, Y.-Y. Yang, C.-Y. Hung, C.-Y. Lin, H.-L. Chen, H.-L. Chou and P.-T. Chou, *Chem. Mater.*, 2016, **28**, 2110–2119.
15 P. P. Das, A. Roy, M. Tathavadekar and P. SujathaDevi, *Appl. Catal., B*, 2017, **203**, 692–703.
16 L. Kavan, J.-H. Yum and M. Graetzel, *Electrochim. Acta*, 2014, **128**, 349–359.
17 M. Janani, P. Srikrishnarka, S. V. Nair and A. S. Nair, *J. Mater. Chem. A*, 2015, **3**, 17914–17938.
18 L. Kavan, H. Krysova, P. Janda, H. Tarabkova, Y. Saygili, M. Freitag, S. M. Zakeeruddin, A. Hagfeldt and M. Grätzel, *Electrochim. Acta*, 2017, **251**, 167–175.
19 P. Kulkarni, S. K. Nataraj, R. G. Balakrishna, D. H. Nagaraju and M. V. Reddy, *J. Mater. Chem. A*, 2017, **5**, 22040–22094.

20 H. Zhang, Y. Wang, P. Liu, S. L. Chou, J. Z. Wang, H. Liu, G. Wang and H. Zhao, *ACS Nano*, 2016, **10**, 507–514.
21 J. Yao, W. Wang, X. Zuo, Q. Yang, M. W. Khan, M. Z. Wu, H. B. Tang, S. W. Jin and G. Li, *Appl. Catal., B*, 2019, **256**, 117857.
22 J. Kwon, V. Ganapathy, Y. H. Kim, K. D. Song, H. G. Park, Y. Jun, P. J. Yoo and J. H. Park, *Nanoscale*, 2013, **5**, 7838–7843.
23 H. Hu, Bu Y. Guan and X. W. Lou, *Chem*, 2016, **1**, 102–113.
24 L. Shen, L. Yu, X. Y. Yu, X. Zhang and X. W. Lou, *Angew. Chem., Int. Ed.*, 2015, **54**, 1868–1872.
25 B. Sun, X. Feng, Y. Yao, Q. Su, W. Ji and C.-T. Au, *ACS Catal.*, 2013, **3**, 3099–3105.
26 L. Shang, H. Yu, X. Huang, T. Bian, R. Shi, Y. Zhao, G. I. Waterhouse, L. Z. Wu, C. H. Tung and T. Zhang, Well-Dispersed ZIF-Derived Co, *Adv. Mater.*, 2016, **28**, 1668–1674.
27 C. Wang, F. Wang, Z. Liu, Y. Zhao, Y. Liu, Q. Yue, H. Zhu, Y. Deng, Y. Wu and D. Zhao, *Nano Energy*, 2017, **41**, 674–680.
28 T. Liu, C. Jiang, B. Cheng, W. You and J. Yu, *J. Mater. Chem. A*, 2017, **5**, 21257–21265.
29 X. Meng, C. Yu, X. Song, Y. Liu, S. Liang, Z. Liu, C. Hao and J. Qiu, *Adv. Energy Mater.*, 2015, **5**, 1500180.
30 J. Yao, K. Zhang, W. Wang, X. Zuo, Q. Yang, H. Tang, M. Wu and G. Li, *ACS Appl. Mater. Interfaces*, 2018, **10**, 19564–19572.
31 C. Yang, M. Y. Gao, Q. B. Zhang, J. R. Zeng, X. T. Li and A. P. Abbott, *Nano Energy*, 2017, **36**, 85–94.
32 D. Guo, X. a. Chen, H. Wei, M. Liu, F. Ding, Z. Yang, K. Yang, S. Wang, X. Xu and S. Huang, *J. Mater. Chem. A*, 2017, **5**, 6245–6256.
33 M. Guo, B. Tang, H. Zhang, S. Yin, W. Jiang, Y. Zhang, M. Li, H. Wang and L. Jiao, *Chem. Commun.*, 2014, **50**, 7356–7358.
34 S. K. Swami, N. Chaturvedi, A. Kumar, R. Kapoor, V. Dutta, J. Frey, T. Moehl, M. Grätzel, S. Mathew and M. K. Nazeeruddin, *J. Power Sources*, 2015, **275**, 80–89.
35 F. Liu, J. Zhu, L. Hu, B. Zhang, J. Yao, M. K. Nazeeruddin, M. Grätzel and S. Dai, *J. Mater. Chem. A*, 2015, **3**, 6315–6323.
36 J. Yao, K. Zhang, W. Wang, X. Zuo, Q. Yang, M. Wu and G. Li, *Electrochim. Acta*, 2018, **279**, 168–176.
37 X. Meng, C. Yu, X. Song, J. Iocozzia, J. Hong, M. Rager, H. Jin, S. Wang, L. Huang, J. Qiu and Z. Lin, *Angew. Chem., Int. Ed.*, 2018, **57**, 4682–4686.
38 Y. Niu, X. Qian, J. Zhang, W. Wu, H. Liu, C. Xu and L. Hou, *J. Mater. Chem. A*, 2018, **6**, 12056–12065.
39 C. Yu, X. Meng, X. Song, S. Liang, Q. Dong, G. Wang, C. Hao, X. Yang, T. Ma, P. M. Ajayan and J. Qiu, *Carbon*, 2016, **100**, 474–483.
40 B. Yang, X. Zuo, P. Chen, L. Zhou, X. Yang, H. Zhang, G. Li, M. Wu, Y. Ma, S. Jin and X. Chen, *ACS Appl. Mater. Interfaces*, 2015, **7**, 137–143.
41 S.-W. Yoon, V.-D. Dao, L. L. Larina, J.-K. Lee and H.-S. Choi, *Carbon*, 2016, **96**, 229–236.
42 P. Zhai, C.-C. Lee, Y.-H. Chang, C. Liu, T.-C. Wei and S.-P. Feng, *ACS Appl. Mater. Interfaces*, 2015, **7**, 2116–2123.
43 H. Jiang, Y. Lin, B. Chen, Y. Zhang, H. Liu, X. Duan, D. Chen and L. Song, *Mater. Today*, 2018, **21**, 602–610.
44 X. Meng, C. Yu, X. Song, Z. Liu, B. Lu, C. Hao and J. Qiu, *J. Mater. Chem. A*, 2017, **5**, 2280–2287.
45 E. Bi, H. Chen, X. Yang, W. Q. Peng, M. Grätzel and L. Y. Han, *Energy Environ. Sci.*, 2014, **7**, 2637–2641.
46 F. Du, X. Zuo, Q. Yang, G. Li, Z. l. Ding, M. Z. Wu, Y. Q. Ma and K. R Zhu, *J. Mater. Chem. C*, 2016, **4**, 10323–10328.
47 J. Deng, L. Yu, D. Deng, X. Q. Chen, F. Yang and X. H. Bao, *J. Mater. Chem. A*, 2013, **1**, 14868–14873.
48 J. D. Roy-Mayhew, D. J. Bozym, C. Punckt and I. A. Aksay, *ACS Nano*, 2010, **4**, 6203–6211.
49 W. P. R. Liyanage, J. S. Wilson, E. C. Kinzel, B. K. Durant and M. Nath, *Sol. Energy Mater. Sol. Cells*, 2015, **133**, 260–267.
50 W. Wang, J. Yao, X. Zuo, Q. Yang, M. Z. Wu, H. B. Tang, S. W. Jin and G. Li, *Nanoscale Horiz.*, 2019, **4**, 1211–1220.
51 A. Shrestha, M. Batmunkh and C. J. Shearer, *Adv. Energy Mater.*, 2017, **7**, 1602276.
52 Z. S. Wu, A. Winter, L. Chen, *et al.*, *Adv. Mater.*, 2012, **24**, 5130–5135.
53 Y. Wang, A. J. Page, Y. Nishimoto, H. J. Qian, K. J. Morokuma and S. Irle, *J. Am. Chem. Soc.*, 2011, **133**, 18837–18842.
54 N. A. Karim, U. Mehmood, H. F. Zahid and T. Asif, *Sol. Energy*, 2019, **185**, 165–188.
55 A. Ashraf, Y. Wu, M. C. Wang, K. Yong, T. Sun, Y. H Jing, R. T. Haasch, N. R. Aluru and S. W. Nam, *Nano Lett.*, 2016, **16**, 4708–4712.

